Measuring the Permittivity and Permeability of a Sample at K_a Band Using a Partially Filled Waveguide

John M. Jarem, *Senior Member, IEEE,* James B. Johnson, Jr., *Member, IEEE,* and W. Scott Albritton, *Member, IEEE*

***Abstract*—A novel method of measuring the relative complex permittivity ($\varepsilon = \varepsilon' - j\varepsilon''$) and relative complex permeability ($\mu = \mu' - j\mu''$) of a material at K_a Band (26.5–40 GHz) using a partially filled waveguide (PFW) (rectangular) and a vector network analyzer (VNA) is presented. The method is based on 1) placing a material sample of length $\tilde{L}$, width $\tilde{a}$ (waveguide width), and height $\tilde{d} \leq \tilde{b}$ ($\tilde{b}$ is the waveguide height) in a rectangular waveguide, 2) measuring the S-parameters of the sample using the VNA, and 3) inferring the $\varepsilon', \varepsilon'', \mu'$, and μ'' parameters by comparing the experimental S-parameters with numerically generated S-parameters. The paper presents a method of moments analysis and also a variational formulation of the scattering that occurs from a finite length sample that partially fills a waveguide. Formulas to calculate the complex Poynting power and energy in the waveguide are derived to check the degree to which the numerical solutions obey the conservation of complex power. Numerical methods to extract the material parameters from the S-parameter data are proposed. The experimental PFW S-parameters of a radar absorbing material are measured and its dielectric material parameters are inferred.**

I. Introduction

AN IMPORTANT problem in microwave and millimeter wave theory [1]–[24] concerns the determination of the values of the complex relative dielectric permittivity, $\varepsilon = \varepsilon' - j\varepsilon''$, and complex relative magnetic permeability, $\mu = \mu' - j\mu''$, of a material in K_a (26.5–40 GHz) and W bands (75–110 GHz). This problem has important applications for biological tissue analysis, radar imaging of terrain (desert and forest) and design of radar absorbing materials (RAM). At the present time, there are several techniques for measuring ε and μ. These are 1) placing a material sample in a millimeter wave cavity and measuring the perturbed quality factor of the cavity and from this determining the ε and μ of the sample [1]; 2) placing a uniform layer of given thickness of sample in free space, illuminating the sample with a normally incident plane wave and from its transmission and reflection coefficients (or S (scattering) parameters (S_{11}, S_{12})) [2]–[8], determining the sample's ε and μ; 3) placing a sample of material of length $\tilde{L}$ in a waveguide (the material fills completely the waveguide's transverse cross-section) illuminating the material with a TE_{10} mode, and from the reflection and transmission coefficients (S_{11}, S_{21}) inferring the ε and μ of the sample [9]–[12]; 4) placing the sample near an open-ended TEM probe and from the measurements inferring the material properties [13]; 5) use of an open-ended Fabry-Perot resonator [14]; and 6) use of a Fourier transform spectroscopy [14]. Ref. [14] gives a survey of current near millimeter wave measurement technology as applied to determination of the absorption coefficient and index of refraction of a material.

Because of the high frequencies and small wavelengths of $K_a(\lambda \cong 8$ mm) and $W(\lambda \cong 3$ mm) bands, all the methods mentioned above have some limitations for measuring the permittivity and permeability of a given sample. The quality factor method requires a cavity roughly 10 mm on a side, and a sample of 1 or 2 mm in cross-section. Also extremely precise dimensions of the cavity feed probe are required, along with knowledge of the probe's effect on the quality factor measurement. The free space layer measurement is limited at K_a and W bands because the layer requires accurate alignment of the normally incident wave, and requires an accurate uniform thickness of the layer over a large transverse area for the magnitude and phase (S_{11} and S_{21}) of the reflection and transmission coefficients to be measured accurately. Unless the sample's dielectric parameters are spatially very uniform, the measurement also only gives an average value of ε and μ in the sample. If the sample consists of large permittivity and permeability values, very thin sample layers are required over a fairly large areas (10 cm $\times$ 10 cm). The S-parameter waveguide method is also limited at K_a and W bands because it is difficult to place a thin sample in the cross-section of the waveguide and have it be exactly perpendicular with its flat surface exactly normal to the longitudinal waveguide axis. Very slight misalignment of the sample, particularly if the sample is of high dielectric value, can cause large error in the magnitude and phase of the reflection coefficients, thus causing nonrepeatability in the data collection process. If the sample is of high dielectric value, a very small change in the sample's length can cause a large change in the sample's reflection and transmission coefficients.

The purpose of this paper is to propose a novel method of measuring the complex permittivity and permeability of a material sample using partially filled waveguide (PFW) theory [1], [15]–[16] and method of moments (MOM) theory. The novel method consists of partially filling a rectangular waveguide with a material sample of length $\tilde{L}$, width $\tilde{a}$, and height

Manuscript received October 3, 1994; revised August 29, 1995.

J. M. Jarem is with the Department of Electrical and Computer Engineering, University of Alabama, Huntsville, AL 35899 USA.

J. B. Johnson, Jr., is with the U.S. Army Redstone Technical Test Center, Redstone Arsenal, AL 35898 USA.

W. S. Albritton is with the Amtec Corp., Huntsville, AL 35805 USA.

IEEE Log Number 9415556.

$\tilde{d}$, ($\tilde{d} < \tilde{b}, \tilde{b} =$ waveguide height), illuminating the sample with a TE_{10} mode and from these experimentally measured reflection and transmission coefficients (S_{11}, S_{21} parameters) inferring the ε and μ of the sample. The ε', ε'', μ', and μ'' of the sample are inferred by using a PFW, MOM analysis to calculate the S_{11} and S_{21} parameters of a material sample of a given (ε', ε'', μ', and μ'') and then least-squares curve fitting these S-parameters to the measured S-parameter data. The proposed PFW method represents a generalization of the filled waveguide (FW) method presented by [9]–[12], which depends on a TE_{10} analysis for the parameter determination.

The authors feel that this is a useful way to measure ε and μ at K_a and W bands for several reasons. First, as the height, $\tilde{d}$, of the sample is reduced, it requires a larger sample length, $\tilde{L}$, to observe significant reflection (S_{11}) and transmission coefficients (S_{21}), as compared with the FW method. Thus at K_a and W bands, the height, $\tilde{d}$, can be reduced until a comfortable working length, $\tilde{L}$, of the sample (10 mm to 25 mm) can be obtained. This is much easier to work with than short length samples. Second, the proposed waveguide method allows measurement of the S-parameters over a wide range of height values, thus supplying a large amount of measurement data from which to determine ε and μ. Each different partially filled height, $\tilde{d}$, exposes the sample to EM radiation in a different and unique way to every other waveguide height. The accumulation of data in this way adds to the certainty of the final answer. Third, placing the sample in a waveguide which is partially filled, the lower waveguide wall is a natural mechanical support for the sample.

The numerical solution presented here is closely related to Strube and Arndt's [17] analysis of a shielded dielectric image guide. Ref. [17] analyzed the reflection that occurred when a TE_{10} mode was incident on a semi-infinite section of dielectric image line. The work presented here is a limiting case of when the image line of [17] fully fills the waveguide transversely. However, in [17] the length of the image line is semi-infinite, whereas in the present analysis a finite length is analyzed. The authors feel that the solution presented here represents an interesting limiting test case for the image line transition presented in [17]. In other words, the solution of [17] should approach the solution presented here when the width of dielectric image line approaches the width of the waveguide (and $\tilde{L} \rightarrow \infty$).

II. Method of Moments Solution

The determination of the electromagnetic fields that result when a TE_{10} waveguide mode (the only propagating mode) is incident on a slab of material whose relative dielectric permittivity is $\varepsilon = \varepsilon' - j\varepsilon''$, whose relative permeability is $\mu = \mu' - j\mu''$, whose width is $\tilde{a}$ (transverse waveguide width), whose length is $\tilde{L}$, and whose height $\tilde{d}$ (Fig. 1 inset) is a three-step procedure that consists of Step 1: determining the forward and backward propagating modes that exist in Regions (a), (b), and (c) of Fig. 1 [Region (b) is composed of Regions (b1) and (b2)]; Step 2: expanding the unknown fields in Regions (a), (b), and (c) in terms of the modes of Step 1 (unknown complex amplitude coefficients are assumed to multiply the modes);

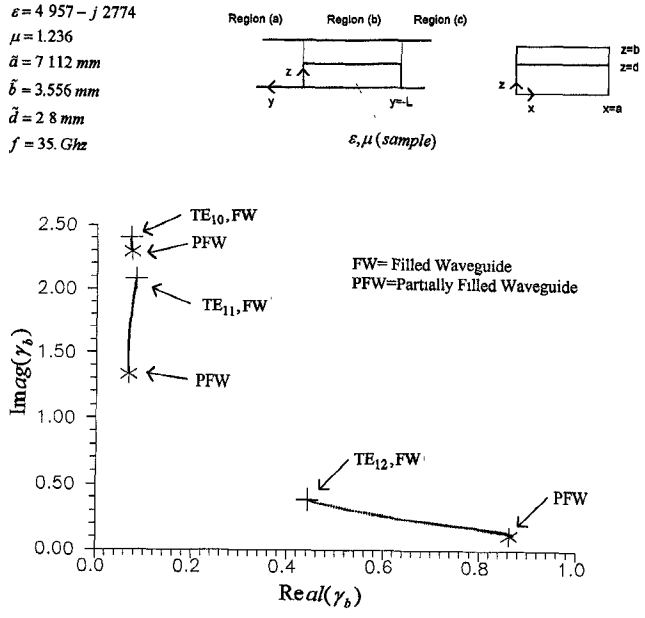

Fig. 1. The values of the first three PFW propagation constants and the values of the first three FW propagation constants are shown. The interconnecting line between the PFW and TE propagation constants shows the intermediate steps used in the search for the PFW propagation constants.

and Step 3: matching electromagnetic boundary conditions at the aperture planes (sample incident side) and $\tilde{y} = -\tilde{L}$ (sample transmit side) to define a matrix equation from which the unknown amplitude coefficients of Step 2 may be solved.

After a lengthy TM_z vector potential analysis of Maxwell's equations in the empty waveguide region of Fig. 1 inset [Regions (a) and (c)], [1], and the partially filled waveguide region of Fig. 1 inset [Region (b)], [1], [15]–[16], the electromagnetic fields of Steps 1 and 2 for Region (a) are

$$E_x^a = \sum_{n=0}^{\infty} q_{na} T_n^a(y) \cos k_x x \sin k_{zn} z,$$

$$E_y^a = \sum_{n=0}^{\infty} p_{na} L_n^a(y) \sin k_x x \sin k_{zn} z,$$

$$E_z^a = \sum_{n=0}^{\infty} T_n^a(y) \sin k_x x \cos k_{zn} z,$$

$$H_x^a = \frac{1}{j\eta_o} \sum_{n=0}^{\infty} s_{na} L_n^a(y) \sin k_x x \cos k_{zn} z,$$

$$H_y^a = \frac{1}{j\eta_o} \sum_{n=0}^{\infty} u_{na} T_n^a(y) \cos k_x x \cos k_{zn} z$$

where $k_x = \dfrac{m\pi}{a}$, $m = 1 \quad k_{zn} = \dfrac{n\pi}{b}$, $n = 0, 1, 2, \ldots$

$$q_{na} = -\frac{k_x k_{zn}}{\mu_a \varepsilon_a - k_{zn}^2}, \quad s_{na} = \frac{-\varepsilon_a \gamma_{an}}{\mu_a \varepsilon_a - k_{zn}^2},$$

$$p_{na} = \frac{k_x q_{na} + k_{zn}}{\gamma_{an}}, \quad u_{na} = \frac{\varepsilon_a k_x}{\mu_a \varepsilon_a - k_{zn}^2}$$

$$\gamma_{an} = \begin{cases} j[\mu_a \varepsilon_a - k_x^2 - k_{zn}^2]^{1/2}, & \mu_a \varepsilon_a - k_x^2 - k_{zn}^2 \geq 0 \\ [k_x^2 + k_{zn}^2 - \mu_a \varepsilon_a]^{1/2}, & \mu_a \varepsilon_a - k_x^2 - k_{zn}^2 < 0, \end{cases}$$

$$n = 0, 1, 2, \ldots$$

$$\eta_o = \sqrt{\frac{\mu_o}{\varepsilon_o}} = 377\,\Omega,\ k_o = \frac{2\pi}{\lambda} = \frac{2\pi f}{c},$$
$$c = 3 \times 10^8 \text{ m/sec}$$
$$f = \text{frequency (Hz)}$$
$$T_{na}(y) = E^I_{na}\delta_{n,o}e^{\gamma_{an}y} + E^R_{na}e^{-\gamma_{an}y},$$
$$L_{na}(y) = E^I_{na}\delta_{n,o}e^{\gamma_{an}y} - E^R_{na}e^{-\gamma_{an}y},$$
$$x = k_o\tilde{x},\quad y = k_o\tilde{y},\quad z = k_o\tilde{z}$$
$$a = k_o\tilde{a},\quad b = k_o\tilde{b},\quad d = k_o\tilde{d},\quad L = k_o\tilde{L},$$
$$\delta_{n,o} = \begin{cases} 1 & n = 0 \\ 0 & n \neq 0. \end{cases} \tag{1}$$

E^I_{na}, $n = 0$ is the amplitude of the incident TE_{10} mode, E^R_{na} are the unknown reflection coefficients which result from the sample located at $y = 0$, μ_a is the relative permeability of Region (a) ($\mu_a = 1$ in this paper), ε_a is the relative permittivity of Region (a) ($\varepsilon_a = 1$ in this paper). x, y, and z are normalized coordinates, and a, b, d, and L are normalized dimensions. All insets are given in terms of normalized coordinates and dimensions.

The solution for Region (c) is given by replacing in (1), a by c and taking $T_{nc}(y)$ and $L_{nc}(y)$ to be

$$T_{nc}(y) = E^T_{nc}e^{\gamma_{cn}(y+L)},\quad L_{nc}(y) = E^T_{nc}e^{\gamma_{cn}(y+L)}. \tag{2}$$

E^T_{nc} are the unknown transmission coefficients which propagate away from $y = -L$ (sample end) in Region (c).

The fields in Region (b) are given by

$$E^b_x = \sum_{n=0}^{\infty} T_{nb}(y)e_{xn}(z)\cos k_x x$$
$$E^b_y = \sum_{n=0}^{\infty} L_{nb}(y)e_{yn}(z)\sin k_x x$$
$$E^b_z = \sum_{n=0}^{\infty} T_{nb}(y)e_{zn}(z)\sin k_x x$$
$$H^b_x = \frac{1}{j\eta_o}\sum_{n=0}^{\infty} L_{nb}(y)h_{xn}(z)\sin k_x x$$
$$H^b_y = \frac{1}{j\eta_o}\sum_{n=0}^{\infty} T_{nb}(y)h_{yn}(z)\cos k_x x$$

where

$$T_{nb}(y) = E^+_{nb}e^{\gamma_{bn}y} + E^-_{nb}e^{-\gamma_{bn}y}$$
$$L_{nb}(y) = E^+_{nb}e^{\gamma_{bn}y} - E^-_{nb}e^{-\gamma_{bn}y}$$

where

$$e_{xn}(z) = \begin{cases} A_{x1n}\sinh\gamma_{z1n}z, & 0 \le z \le d \\ A_{x2n}\sinh\gamma_{z2n}(z-b), & d \le z \le b \end{cases},$$
$$e_{yn}(z) = \begin{cases} A_{y1n}\sinh\gamma_{z1n}z, & 0 \le z \le d \\ A_{y2n}\sinh\gamma_{z2n}(z-b), & d \le z \le b \end{cases}$$
$$e_{zn}(z) = \begin{cases} A_{z1n}\cosh\gamma_{z1n}z, & 0 \le z \le d \\ A_{z2n}\cosh\gamma_{z2n}(z-b), & d \le z \le b \end{cases},$$
$$h_{xn}(z) = \begin{cases} H_{x1n}\cosh\gamma_{z1n}z, & 0 \le z \le d \\ H_{x2n}\cosh\gamma_{z2n}(z-b), & d \le z \le b \end{cases}$$
$$h_{yn}(z) = \begin{cases} H_{y1n}\cosh\gamma_{z1n}z, & 0 \le z \le d \\ H_{y2n}\cosh\gamma_{z2n}(z-b), & d \le z \le b \end{cases}$$

$$A_{x1n} = \left(\frac{\varepsilon_{b2}}{\varepsilon_{b1}}\right)k_x\gamma_{z1n}C_nA_{z2n},\ A_{x2n} = \left(\frac{k_x\gamma_{z2n}}{k_x^2-\gamma_{bn}^2}\right)A_{z2n}$$
$$A_{y1n} = \frac{\varepsilon_{b2}}{\varepsilon_{b1}}\gamma_{bn}\gamma_{z1n}C_nA_{z2n},\ A_{y2n} = \left(\frac{\gamma_{bn}\gamma_{z2n}}{k_x^2-\gamma_{bn}^2}\right)A_{z2n}$$
$$A_{z1n} = \frac{\varepsilon_{b2}}{\varepsilon_{b1}}(k_x^2-\gamma_{bn}^2)C_nA_{z2n},\quad A_{z2n} = 1.$$
$$H_{x1n} = -\varepsilon_{b2}\gamma_{bn}C_nA_{z2n},\quad H_{x2n} = -\varepsilon_{b2}\frac{\gamma_{bn}}{k_x^2-\gamma_{bn}^2}A_{z2n}$$
$$H_{y1n} = \varepsilon_{b2}k_xC_nA_{z2n},\quad H_{y2n} = \frac{\varepsilon_{b2}k_x}{k_x^2-\gamma_{bn}^2}A_{z2n}$$
$$C_n = \frac{1}{k_x^2-\gamma_{bn}^2}\frac{\cosh\gamma_{z2n}(d-b)}{\cosh\gamma_{z1n}d}. \tag{3}$$

E^+_{nb} is the unknown amplitude of the PFW mode traveling to the right and E^-_{nb} is the unknown amplitude of the PFW mode traveling to the left in Region (b). γ_{bn} is the longitudinal propagation constant of the nth PFW mode and satisfies the well known PFW eigenvalue equations

$$\frac{\gamma_{z1n}}{\varepsilon_{b1}}\tanh\gamma_{z1n}d = \frac{\gamma_{z2n}}{\varepsilon_{b2}}\tanh\gamma_{z2n}(d-b) \tag{4a}$$
$$0 = \gamma_{zin}^2 + \gamma_{bn}^2 + \mu_{bi}\varepsilon_{bi},\quad i = 1, 2. \tag{4b}$$

μ_{bi} is the relative complex permeability in Regions (b1) and (b2), respectively, and ε_{bi} is the permittivity in the Regions (b1) and (b2). In this paper $\mu_{b2} = 1$, $\varepsilon_{b2} = 1$. Also $\varepsilon_{b1} = \varepsilon = \varepsilon' - j\varepsilon''$ and $\mu_{b1} = \mu = \mu' - j\mu''$ are the unknown relative permeability and permittivity of the sample which is to be determined.

Three different waveguide modal methods have been tested to numerically enforce EM boundary conditions at the interfaces $y = 0$ and $y = -L$. In the first method, only the E_z and H_x field components were matched at the interfaces; in the second method, the transverse electric and magnetic fields were dotted with themselves and this dot product was matched at the interface (Galerkin method); and in the third method, the E_x, E_z, and H_x field components were all individually matched at the interfaces. In all three methods, enforcement of the boundary condition is imposed by multiplying the field or field components by waveguide modes and integrating the resulting expression over the waveguide cross-section.

The EM boundary conditions in the first and second methods are given by the equations

$$\int_{\text{C.S.}} \vec{e}^{\,T^{a,c}}_{tn} \cdot \vec{E}^{\,a,c}\Big|_{y=0^+,-L^-} dS = \int_{\text{C S.}} \vec{e}^{\,T^{a,c}}_{tn} \cdot \vec{E}^{\,b}\Big|_{y=0^-,-L^+} dS$$
$$\int_{\text{C.S.}} \vec{h}^{\,T^{a,c}}_{tn} \cdot \vec{H}^{\,a,c}\Big|_{y=0^+,-L^-} dS = \int_{\text{C.S.}} \vec{h}^{\,T^{a,c}}_{tn} \cdot \vec{H}^{\,b}\Big|_{y=0^-,-L^+} dS \tag{5}$$

where

$$\vec{e}^{\,T^a}_{tn} = \rho_{na}\cos k_x x\sin k_{zn}z\hat{x} + \sin k_x x\cos k_{zn}z\hat{z}$$
$$\vec{h}^{\,T^a}_{tn} = \sin k_x x\cos k_{zn}z\hat{x} \tag{6}$$

and where $\vec{e}_{tn}^{\,T^a}$ and $\vec{h}_{tn}^{\,T^a}$ are given by (6) with a replaced by c. The boundary matching equations of the first method are given by $\rho_{na} = \rho_{nc} = 0$, and the boundary matching equations of the second method are given by $\rho_{na} = q_{na}$ and $\rho_{nc} = q_{nc}$. Because $\vec{e}_{tn}^{\,T^{a,c}}$ and $\vec{h}_{tn}^{\,T^{a,c}}$ (T = test) involve waveguide sinusoidal modal fields in Region (a), they satisfy the orthogonality relations

$$\int_{\text{C.S.}} \vec{e}_{tn'}^{\,T^{a,c}} \cdot \vec{e}_{tn}^{\,E^{a,c}}\, dS = M_n^{a,c}\delta_{n,n'}$$
$$\int_{\text{C.S.}} \vec{h}_{tn'}^{\,T^{a,c}} \cdot \vec{h}_{tn}^{\,E^{a,c}}\, dS = N_n^{a,c}\delta_{n,n'} \quad n,n' = (0,1,2,\ldots) \tag{7}$$

$$\vec{e}_{tn}^{\,E^a} = q_{na}\cos k_x x \sin k_{zn} z\hat{x} + \sin k_x x \cos k_{zn} z\hat{z}$$
$$\vec{h}_{tn}^{\,E^a} = \sin k_x x \cos k_{zn} z\hat{x} \tag{8}$$

and where $\vec{e}_{tn}^{\,E^c}$ and $\vec{h}_{tn}^{\,E^c}$ are given by (8) with a replaced by c. The matrix equations for the first and second methods for E_{nb}^+ and E_{nb}^- are given by

$$2E_{n'a}^I\delta_{n',o} = \sum_{n=0}^{\infty}\{[I_{Ean',n} + I_{Han',n}]E_{nb}^+ + [I_{Ean',n} - I_{Han',n}]E_{nb}^-\} \tag{9a}$$

$$0 = \sum_{n=0}^{\infty}\{e^{-\gamma_{nb}L}[I_{Ecn',n} - I_{Hcn',n}]E_{nb}^+ + e^{\gamma_{nb}L}[I_{Ecn',n} - I_{Hcn',n}]E_{nb}^-\} \tag{9b}$$

where

$$I_{Ean',n} = \frac{2[\rho_{n'a}I_{exn',n} + I_{ezn',n}]}{b[\rho_{n'a}q_{n'a} + (1+\delta_{o,n'})]}$$
$$I_{Han',n} = \frac{2I_{hxn',n}}{bs_{n'a}[1+\delta_{o,n'}]} \tag{10}$$

where

$$I_{exn',n} = A_{x1n}I_{1ex}(n',n) + A_{x2n}I_{2ex}(n',n)$$
$$I_{ezn',n} = A_{z1n}I_{1ez}(n',n) + A_{z2n}I_{2ez}(n',n)$$
$$I_{hxn',n} = H_{x1n}I_{1ez}(n',n) + H_{x2n}I_{2ez}(n',n)$$
$$I_{1ex}(n',n) = \int_o^d \sin k_{zn'}z \sinh\gamma_{z1n}z\, dz$$
$$I_{2ex}(n',n) = \int_d^b \sin k_{zn'}z \sinh\gamma_{z2n}(z-b)\, dz$$
$$I_{1ez}(n',n) = \int_o^d \cos k_{zn'}z \cosh\gamma_{z1n}z\, dz$$
$$I_{2ez}(n',n) = \int_d^b \cos k_{zn'}z \cosh\gamma_{z2n}(z-b)\, dz. \tag{11}$$

The $I_{Ecn',n}$ and $I_{Hcn',n}$ terms are found replacing a by c in (10). Once E_{nb}^+ and E_{nb}^- are determined, (1)–(3) may be used to find E_{na}^R and E_{nc}^T.

The third method of matching boundary conditions is the method used by [17] to match EM fields for the dielectric image line-rectangular waveguide transition interface. There is a significant difference in the boundary matching of the present problem and that of the dielectric image line. In the problem of [17], it was possible to 1) choose the number of waveguide modes used for expansion (longitudinal TE and TM rectangular waveguide modes) and the number of dielectric image line hybrid modes used for expansion equal to one another; and 2) enforce (that is multiply each EM field component by the proper waveguide modal function and integrate across the waveguide cross section) the tangential boundary conditions of each EM field component using the rectangular waveguide modes as test functions. In the present problem, it was not possible to do this because the waveguide expansion functions consisted of N_w TM_z rectangular waveguide modes (mode number $n = 0$, $N_w - 1$) in Region (a) and N_w TM_z rectangular waveguide modes in Region (c). At each interface there were $N_w - 1 E_x$ rectangular waveguide modal coefficient equations, $N_w E_z$ rectangular waveguide modal coefficient equations and $N_w H_x$ rectangular waveguide modal coefficient equations that had to be enforced. With two interfaces, this led to $2(3N_w - 1)$ rectangular waveguide modal coefficient equations that had to be satisfied. For a square matrix equation which was analyzed in this paper, it was necessary to choose $2(3N_w - 1) - 2N_w = 4N_w - 2$ forward and backward PFW waveguide modes as expansion functions. This choice made the number of PFW expansion functions $4N_w - 2$ unequal to the number rectangular waveguide expansion functions $2N_w$.

All three boundary matching methods were tested numerically (for $\mu_a = \mu_c = 1$, $\varepsilon_a = \varepsilon_c = 1$) on a number of different parameter cases (different L, ε, μ, d). It was found that the third method gave extremely poor, unusable numerical results when the matrix equation was solved. It was also found that the $\rho_{na} = \rho_{nc} = 0$ set of values gave far more accurate complex power conservation results and far more accurate matching of the aperture fields than did the Galerkin values of $\rho_{na} = q_{na}$, $\rho_{nc} = q_{nc}$. For this reason, the first method, that is the $\rho_{na} = \rho_{nc} = 0$ values, have been used in all calculations in this paper. Because of the extremely poor numerical results as found by the third method and because this is the boundary matching method used by [17], the authors believe that the present problem cannot be treated as simply a limiting case of the rigorous dielectric image line analysis as presented in [17].

Using the first method of boundary matching, $\rho_{na} = \rho_{nc} = 0$, the S-parameters are calculated using (9) from the equation

$$S_{11} = \frac{E_{oa}^R}{E_{oa}^I}, \qquad S_{21} = \frac{E_{oc}^T}{E_{oa}^I} \tag{12}$$

provided $\varepsilon_a = \varepsilon_c = 1$, $\mu_a = \mu_c = 1$. Because the sample is isotropic, we note that $S_{22} = S_{11}$ and $S_{12} = S_{21}$.

To cross-check the numerical MOM results of (9a) and (9b), the authors have also derived a variational expression (Section III) for the admittance of the sample Y_S, ($Y_S = \frac{1-R}{1+R}$ where $R = E_{oa}^R$). The admittance Y_S is referenced at the $y = 0$ plane. It turned out that the variational admittance expression depended only on matching of the E_z and H_x EM fields at the $y = 0, -L$ interfaces for its derivation. Based on this information, the authors believe that the $\rho_{na} = \rho_{nc} = 0$ values (which correspond to only E_z and H_x matching at $y = 0, -L$) give better numerical results than the Galerkin values $\rho_{na} = q_{na}$, $\rho_{nc} = q_{nc}$ (which correspond to matching of a linear combination of the fields E_x and E_z, and matching

of the H_x field) because the $\rho_{na} = q_{na}$, $\rho_{nc} = q_{nc}$ values cause a larger error in the E_z field than do the $\rho_{na} = 0$, $\rho_{nc} = 0$ values because both the E_x and E_z are being forced to equality when the $\rho_{na} = q_{na}$, $\rho_{nc} = q_{nc}$ values are used rather than only the E_z field alone, as occurs when the $\rho_{na} = 0$, $\rho_{nc} = 0$ values are used. The larger error in the E_z field, as occurs in the Galerkin case, thus causes overall worse numerical performance than the $\rho_{na} = \rho_{nc} = 0$ testing values.

There are two important numerical cross-checks that can be made of the formulation as given in (1)–(11). The first involves the calculation of the eigenfunctions e_{zn} of h_{xn} (3). Collin [18] has shown that for a transversely inhomogeneous and anisotropic waveguide, from the reciprocity theorem, that if $\vec{E}_n$ and $\vec{H}_m$ are two PFW modes, then

$$\int_{\text{C.S.}} \vec{E}_n \, x \, \vec{H}_m \cdot \hat{a}_z \, dS = 0 \tag{13}$$

when $\gamma_m \neq \gamma_n$. Substituting different modes from (3), we find that above equation reduces to

$$0 = A_{z1n}H_{x1m} \int_o^d \cosh \gamma_{z1n} z \cosh \gamma_{z1m} z \, dz + A_{z2n}H_{x2m} \int_d^b \cosh \gamma_{z2n}(z-b) \cosh \gamma_{z2m}(z-b) \, dz \qquad \gamma_{bm} \neq \gamma_{bn} \tag{14}$$

where all constants are given previously. Extensive numerical testing of (14) has verified the above orthogonality equation to a high degree of accuracy.

The second numerical cross-check involves the numerical accuracy of the MOM solution as given in (9). The accuracy of the numerical solution may be checked by comparing the complex Poynting power that flows across the interfaces $y = 0$ and $y = -L$ as calculated by the Region (a), (b), and (c) solutions. After algebra, it is found that complex power $P_C(y) = P_R(y) + jP_X(y) = \frac{1}{2}\int_{\text{C.S.}} \vec{E}\,(y) \times \vec{H}^*(y) \cdot (-\hat{a}_y dS)$ at a plane

1) $y > 0$ in Region (a) is given by

$$P_C(y) = -\frac{jb}{2} F \sum_{n=0}^{\infty} s_{na}^* T_{na}(y) L_{na}^*(y)(1 + \delta_{o,n}) \tag{15}$$

2) $-L < y < 0$ in Region (b)

$$P_C(y) = -jF \sum_{n=0}^{\infty} \sum_{n'=0}^{\infty} T_{bn'}(y) L_{bn}^*(y) I_{\text{EH}}(n', n) \tag{16}$$

3) $y < -L$ in Region (c)

$$P_C(y) = -\frac{jb}{2} F \sum_{n=0}^{\infty} s_{nc}^* T_{nc}(y) L_{nc}^*(y)(1 + \delta_{o,n}) \tag{17}$$

where $F = \frac{a}{4\eta_o k_o^2}$

$$I_{EH}(n', n) = A_{z1n'}H_{x1n}^* \int_o^d \cosh \gamma_{z1n'} z \cosh \gamma_{z1n}^* z \, dz + A_{z2n'}H_{x2n}^* \int_d^b \cosh \gamma_{z2n'}(z-b) \cosh \gamma_{z2n}^*(z-b) \, dz. \tag{18}$$

The accuracy of complex power matching from the numerical solution at $y = 0$ and $y = -L$ was measured by the normalized power error equation

$$P_{err} = [|P_C(0^+) - P_C(0^-)| + |P_C(-L^+) - P_C(-L^-)|]/P_{INC} \tag{19}$$

where

$$P_{\text{INC}} = F \frac{b\beta_{ao}}{\mu_a} \left| E_{oa}^I \right|^2, \quad \beta_{ao} = \frac{\gamma_{ao}}{j}. \tag{20}$$

P_{INC} is the power of the TE_{10} incident mode.

III. Variational Solution

Instead of the MOM, an alternative method of determining the S-parameters and EM fields of a finite length, partially filled waveguide sample, is to form a TE_{10} aperture admittance variational expression on the input side of the material ($y = 0$), and using this expression extremalize the resulting expression to determine the reflection coefficients of the sample and from this the EM fields of the system. We use a similar variational analysis as presented by Galejs [19] to determine the aperture TE_{10} admittance of a rectangular waveguide feeding a ground plane aperture.

To begin the analysis, we evaluate the E_z electric field at $y = 0^+$ [Region (a)]. We find

$$E_{zA}(z) = E_z^a(x, z, o^+)/\sin k_x x = a_o(1 + R) + \sum_{n=1}^{\infty} a_n \cos k_{zn} z \tag{21}$$

where $R = E_{oa}^R/E_{oa}^I$ is the TE_{10} [Region (a)] reflection coefficient, $a_o = \frac{1}{b(1+R)} \int_o^b E_{zA}(z) \, dz$, $a_n = \frac{2}{b} \int_o^b E_{zA}(z) \cos k_{zn} z \, dz$, $n = 1, 2, 3, \ldots$. At $y = 0^-$, we find

$$E_{zA} = E_z^b(x, z, o^-)/\sin k_x x = \sum_{n=0}^{\infty} (E_{nb}^+ + E_{nb}^-) e_{zn}(z). \tag{22}$$

If this equation is multiplied by $h_{xn}(z)$ and integrated from 0 to b, and the orthogonality property of (14) is used, it is found

$$E_{nb}^+ + E_{nb}^- = \frac{1}{N_{bn}} \int_o^b h_{xn}(z) E_{zA}(z) \, dz, \qquad N_{bn} = \int_o^b e_{zn}(z) h_{xn}(z) \, dz. \tag{23}$$

After equating the H_x field at $y = 0^+$ and $y = 0^-$, we find

$$s_{oa} a_o (1 - R) + \sum_{n'=1}^{\infty} s_{n'a}(-a_{n'}) \cos k_z z = \sum_{n'=0}^{\infty} (E_{n'b}^+ - E_{n'b}^-) h_{xn'}(z). \tag{24}$$

At this point, it is convenient to use matrix notation. Using (23), we may express $\underline{E}^-$ in terms of $\underline{E}^+$ and after letting

$\underline{E}^{+t} = [E^+_{0b}, E^+_{1b}, \ldots]$, $\underline{E}^{-t} = [E^-_{0b}, E^-_{1b}, \ldots]$ we find from (9) and (10) ($\rho_{n'a} = \rho_{n'c} = 0$)

$$\underline{E}^- = \underline{\underline{K}}_2^{-1}\underline{\underline{K}}_1\underline{E}^+ = \underline{\underline{R}}_b\underline{E}^+$$
$$\underline{\underline{K}}_1 = [e^{-\gamma_{bn}L}(I_{Ecn',n} - I_{Hcn',n})],$$
$$\underline{\underline{K}}_2 = [-e^{\gamma_{bn}L}(I_{Ecn',n} + I_{Hcn',n})]. \quad (25)$$

The -1 superscript means matrix inverse and the t superscript means transpose.

After expressing (23) in matrix form, we find $\underline{E}^+ = \int_o^b E_{zA}(z')[\underline{\underline{I}} + \underline{\underline{R}}_b]^{-1}\ \underline{\underline{N}}_b^{-1}\underline{h}_x(z')\ dz'$ where $\underline{\underline{N}}_b^{-1} = [(1/N_{bn})\delta_{n,n'}]$ $\underline{\underline{I}} = [\delta_{n,n'}]$, and $\underline{h}_x^t(z')' = [h_{x0}(z'),\ h_{x1}(z'), \ldots]$. Substituting a_0, a_n, $E^-_{n'b}$, and $E^+_{n'b}$ from (21)–(25), respectively, (24) may be expressed in terms of the $E_{zA}(z)$. We have

$$s_{oa}\frac{1}{b}\frac{(1-R)}{(1+R)}\int_o^b E_{zA}(z)\ dz = \int_o^b E_{zA}(z') \times \left\{\sum_{n=1}^{\infty}\frac{2s_{na}}{b}\cos k_{zn}z\cos k_{zn}z' + \underline{h}_x^t(z')\underline{\underline{A}}\,\underline{h}_x(z)\right\} \quad (26)$$

where $\underline{\underline{A}} = \underline{\underline{N}}_b^{-1}\ [\underline{\underline{I}} + \underline{\underline{R}}_b]^{-1^t}\ [\underline{\underline{I}} - \underline{\underline{R}}_b]^t$. If we multiply the above equation by $E_{zA}(z)$, integrate from 0 to b (following [19]), and perform a small amount of algebra, we find

$$Y_S = \frac{(1-R)}{(1+R)} = \frac{\int_0^b\int_0^b E_{zA}(z)E_{zA}(z')G(z,z')dz'dz}{D^2} \quad (27)$$

where $G(z,z') = G_1(z,z') + \frac{1}{2}[G_{2a}(z,z') + G_{2a}(z,z')]$, $G_1(z,z') = \sum_{n=1}^{\infty}\frac{2s_{na}}{s_{oa}}\cos k_{zn}z\cos k_{zn}z'$, $G_{2a}(z,z') = \frac{b}{s_{oa}}\underline{h}_x^t(z')\underline{\underline{A}}\,\underline{h}_x(z)$, $D = \int_0^b E_{zA}dz$.

Galejs [19] shows that the above expression, because the function $G(z,z')$ is symmetric in z and z', produces an admittance $Y_s = \frac{1-R}{1+R}$, which is stationary or insensitive to small error in the aperture field $E_{zA}(z)$.

Equation (27) for Y_s may be extremalized by expanding

$$E_{zA}(z) = E_0 + \sum_{n=1}^{\infty}E_n\cos k_{zn}z = E_0\left[1 + \sum_{n=1}^{\infty}e_n\cos k_{zn}z\right] \quad (28)$$

where

$$e_n = E_n/E_0.$$

Substituting this expression into (27) and then setting $\frac{\partial Y_s}{\partial e_n} = 0$ for $n = 1, 2, \ldots$, the aperture admittance using the above $E_{zA}(z)$ expression is given by

$$Y_s = \sum_{n=1}^{\infty}\zeta_n e_n^2 + \sum_{n'=0}^{\infty}\sum_{n''=0}^{\infty}K_{n',n''}e_{n'}e_{n''} \quad (29)$$

where $\zeta_n = \frac{s_{na}}{2s_{oa}}$, $K_{n',n''} = \frac{1}{2bs_{oa}}[\underline{h}^t_{xn''}\underline{\underline{A}}\,\underline{h}_{xn'} + \underline{h}^t_{xn'}\underline{\underline{A}}\,\underline{h}_{xn''}]$, $\underline{h}^t_{xn} = [\int_0^b h_{x0}(z)\cos k_{zn}zdz,\ \int_0^b h_{x1}(z)\cos k_{zn}zdz, \ldots]$. After differentiation, the final matrix equation to determine e_n is given by

$$-K_{n',0} = \sum_{n''=1}^{\infty}[\zeta_{n'}\delta_{n',n''} + K_{n',n''}]e_{n''}. \quad (30)$$

The reflection coefficient R is determined by $R = \frac{1-Y_s}{1+Y_s}$, and Y_s is determined from (27) using the e_n as results from (30) substituted in it. When the sample extends to infinity ($L = \infty$), $\underline{\underline{R}}_b = 0$.

IV. Material Parameter (ε', ε'', μ', μ'') Analysis

The sample material parameters $\varepsilon = \varepsilon' - j\varepsilon''$ and $\mu = \mu' - j\mu''$ (Fig. 1 inset) may be determined from laboratory S-parameter measurement data (collected over a suitable range of sample lengths, $\tilde{L}$, and sample heights $\tilde{d}$, using the MOM solution of (9) (or variational solution) in two ways.

First, an S-parameter error function between the measured complex S-parameter data (S^M_{11}, S^M_{21}) and the numerically calculated complex S-parameter data (S_{11}, S_{21}) is minimized with respect to four independent variables (ε', ε'', μ', and μ'') to find the values of ε', ε'', μ', and μ'' which most closely correspond to that of the measured sample. When the magnitude and phase of the S-parameters can be measured accurately, a useful error function to obtain the sample parameters is given by the S-parameter error function

$$S^{\text{err}}(\varepsilon',\ \varepsilon'',\ \mu',\ \mu'') = \sum_{i=1}^{I}\sum_{i'=1}^{I'}\{|S^M_{11}(d_i,\ L_{i'}) - S_{11}(d_i,\ L_{i'},\ \varepsilon',\ \varepsilon'',\ \mu',\ \mu'')|^2 + |S^M_{21}(d_i,\ L_{i'}) - S_{21}(d_i,\ L_{i'},\ \varepsilon',\ \varepsilon'',\ \mu',\ \mu'')|^2\}. \quad (31)$$

When the S-parameter data (magnitude and phase) is noisy, an alternative error function that can be used is one which is based on the normalized power that is absorbed (as heat) in the sample. The normalized power absorbed is the power absorbed by the sample, divided by the incident power of the TE_{10} mode. The power absorbed error function is given by

$$P^{\text{err}}_{AN} = \sum_{i=1}^{I}\sum_{i'=1}^{I'}[P^M_{AN}(d_i,\ L_{i'}) - P_{AN}(d_i,\ L_{i'},\ \varepsilon',\ \varepsilon'',\ \mu',\ \mu'')]^2 \quad (32)$$

where

$$P_{AN}(d,\ L) = 1 - |S_{11}|^2 - |S_{21}|^2. \quad (33)$$

In the present paper, S_{11} and S_{21} have been calculated for a given (ε', ε'', μ', and μ'') by (1)–(12), and S^{err} and P^{err}_{AN} has been minimized by the IMSL package BCONF.

A second way that the parameters (ε', ε'', μ', and μ'') of the sample can be determined involves the use of the complex Poynting theorem. Assuming that the incident TE_{10} mode arises from a source at $y = \infty$, the complex Poynting theorem as applied to the volume, $V(V = V_{b1} + V_{\text{ext}})$ and the surface,

S (S encloses V), (Fig. 9 inset) assumes the form

$$P_S = 0 = \oint \frac{1}{2} \vec{E} \times \vec{H}^* \cdot \hat{a}_n \, dS + P_d + j2\omega(\bar{W}_M - \bar{W}_E) \quad (34)$$

where

$$P_d = P_{de} + P_{dm}$$

$$P_{de} = \frac{1}{2}\omega\varepsilon_0\varepsilon'' \int_{V_{b1}} \vec{E}^{b1} \cdot \vec{E}^{b1*} \, dV$$

$$P_{dm} = \frac{1}{2}\omega\mu_0\mu'' \int_{V_{b1}} \vec{H}^{b1} \cdot \vec{H}^{b1*} \, dV$$

$$\bar{W}_M = \frac{\mu_0}{4}\left[\mu' \int_{V_{b1}} \vec{H}^{b1} \cdot \vec{H}^{b1*} \, dV + \int_{V_{\text{ext}}} \mu'_{\text{ext}} \vec{H} \cdot \vec{H}^* \, dV\right]$$

$$\bar{W}_E = \frac{\varepsilon_0}{4}\left[\varepsilon' \int_{V_{b1}} \vec{E}^{b1} \cdot \vec{E}^{b1^*} \, dV + \int^{V_{\text{ext}}} \varepsilon'_{\text{ext}} \vec{E} \cdot \vec{E}^* \, dV\right]$$

where V_{b1} is the volume over the sample, V_{ext} is a region in V but exterior to V_{b1}, P_{de}, and P_{dm} represent the time-averaged electric and magnetic power which is dissipated in the sample (this is the only place in the system where energy is dissipated), and $\overline{W}_M$ and $\overline{W}_E$ represent the time-averaged magnetic and electric energies stored in the volume, V. In all calculations in this paper, the μ'_{ext} and $\varepsilon'_{\text{ext}}$ of the V_{ext} region is assumed to be 1. If Regions (a), (b2), and (c) were different from free space, then the appropriate μ'_{ext} and $\varepsilon'_{\text{ext}}$ would have to be evaluated there, also $P_S = 0$ as there are no sources of power in volume V.

The closed surface integral is integrated over the two end faces (Fig. 9 inset) (located at $y = \ell\lambda_g/2$ and $y = -L - \ell'\lambda_g/2$) and over the waveguide walls. ℓ and ℓ' are large positive integers and λ_y is the normalized guide wavelength of the TE_{10} propagating mode which exists in Regions (a) and (c). The integers ℓ and ℓ' are chosen to be large enough that the evanescent fields of the interfaces at $y = 0$ and $y = -L$ make a negligible contribution to the end faces of S at $y = \frac{\ell\lambda_g}{2}$ and $y = -L - \frac{-\ell'\lambda_g}{2}$. Because the waveguide walls are perfect conductors and the tangential electric field there is zero, no contribution to the closed surface integral is made by the waveguide walls.

Because the waveguide walls make no contribution to the closed surface integral and because the evanescent fields in Regions (a) and (c) don't contribute to closed surface integral over V, (because the end faces are far from the sample interfaces), the value of the entire closed surface integral only depends on the incident (E^I_{oa}), reflection ($S_{11}E^I_{oa}$), and transmission ($S_{21}E^I_{oa}$) wave amplitudes of the propagating TE_{10} modes of the system. Thus the entire surface integral is a quantity that can be expressed in terms of the measurable S-parameters, S_{11} and S_{21}.

After evaluation of the known closed surface integral (real and imaginary parts) in terms of the measured S-parameters and evaluating the energy integrals of (34) in Regions (a) and (c), then expressing these integrals in terms of integrals over the evanescent electric fields evaluated at the interfaces, and after extensive algebra, it is found that the real and imaginary parts of (34) give

$$F[\mu'' I_{H1} + \varepsilon'' I_{E1}] = F\frac{\beta_{ao}b}{\mu_a}|E^I_{oa}|^2[1 - |S_{11}|^2 - |S_{21}|^2] = P_{\text{INC}}P_{AN} \quad (35a)$$

$$\begin{aligned} F[\mu' I_{H1} - \varepsilon' I_{E1}] &= F\Bigg\{ - [\mu'_{b2} I_{H2} - \varepsilon'_{b2} I_{E2}] \\ &\quad - \text{I mag}\left\{\frac{\text{jb}}{2}\sum_{\text{n=1}}^{\infty} \text{s}^*_{\text{na}}\,\text{T}_{\text{na}}(0^+)\text{L}^*_{\text{na}}(0^+)\right\} \\ &\quad - \text{I mag}\left\{ - \frac{\text{jb}}{2}\sum_{\text{n=1}}^{\infty} \text{s}^*_{\text{nc}}\,\text{T}^*_{\text{nc}}(-\text{L}^-)\text{L}^*_{\text{nc}}(-\text{L}^-)\right\} \\ &\quad + \frac{2\beta_{ao}b}{\mu_a}|S_{11}|\sin\theta_{11}|E^I_{oa}|^2\Bigg\} \\ &= P_{INC}W_N = P_{\text{INC}}(W_N^{\text{num}} + W_N^{\text{spar}}) \end{aligned} \quad (35b)$$

where $\mu'_{b2} = 1$, $\varepsilon'_{b2} = 1$, $S_{11} = |S_{11}|e^{j\theta_{11}}$

$$\begin{aligned} I_{Ei} = \sum_{n=0}^{\infty}\sum_{n'=0}^{\infty} \{ & [A_{xin}A^*_{xin'}I_{ssi}(n,n') \\ & + A_{zin}A^*_{zin'}I_{cci}(n,n')]I_{TT}(n,n') \\ & + A_{yin}A^*_{yin'}I_{ssi}(n,n')I_{LL}(n,n')\} \end{aligned}$$

$$\begin{aligned} I_{Hi} = \sum_{n=0}^{\infty}\sum_{n'=0}^{\infty} \{ & H_{xin}H^*_{xin'}I_{LL}(n,n') \\ & + H_{yin}H^*_{yin'}I_{TT}(n,n')\}I_{cci}(n,n'),\ i = 1,2 \end{aligned}$$

$$I_{cc1}(n,\ n') = \int_o^d \cosh\gamma_{z1n}z\cosh\gamma^*_{z1n'}z \ \ dz$$

$$I_{cc2}(n,\ n') = \int_d^b \cosh\gamma_{z2n}(z-b)\cosh\gamma^*_{z2n'}(z-b) \ \ dz.$$

$I_{ssi}(n,n')$, $i = 1,2$ is given by with sinh (hyperbolic sine) replacing the cosh (hyperbolic cosine) in these terms. Also in (35)

$$I_{TT}(n,n') = \int_{-L}^{o} T_{nb}(y)T^*_{n'b}(y)\ dy,$$

$$I_{LL}(n,n') = \int_{-L}^{o} L_{nb}(y)L^*_{n'b}(y)\ dy.$$

The I_{Ei} and I_{Hi} ($i = 1,2$) integrals come from the volume integrals $\int_V \vec{E}\cdot\vec{E}^* \ d\tilde{V}$ and $\int_V \vec{H}\cdot\vec{H}^* \ d\tilde{V}$ which occur in (34). Imag{} means the imaginary part. The sums in (35b) are summed over the evanescent modes in the aperture. This is why the sum of these terms starts at $n = 1$. The term W_N^{spar} in (35b) refers to S-parameter term in the right hand side (RHS) of (35b) and W_N^{num} (num refers to numerical, N refers to normalized by incident power) refers to the other terms in the RHS of (35b). If (35a–b) are divided by P_{inc} (therefore

normalized) and we let $I_{EN} = I_{E1}$ and $I_{HN} = I_{H1}/P_{INC}$, (35a–b) become

$$\mu' I_{HN}(d,L) + \varepsilon'' I_{EN}(d,L) = P_{AN}(d,L) \tag{36a}$$

$$\mu' I_{HN}(d,L) - \varepsilon' I_{EN}(d,L) = W_N(d,L) = W_N^{\text{num}}(d,L) + W_N^{\text{spar}}(d,L). \tag{36b}$$

If (36a) is evaluated using two distinct values of the ordered pair (d, L) (that is, evaluated at $(d_1, L_1) \neq (d_2, L_2)$), a 2×2 set of nonlinear equations is produced from which μ'' and ε'' can be inverted. If (36b) is evaluated at two distinct values of (d, L), (36b) produces a 2×2 set of nonlinear equations from which μ' and ε' can be inverted. The explicit way μ'' and ε'' occur in (36a) is suggestive of using an approximate 2×2 linear determination of μ'' and ε'' in (36a), with the I_{HN}, I_{EN}, and P_{AN} of (36a) approximated by values close to the true values of μ'' and ε'' in (36a). The same applies to the determination of μ' and ε' in (36b). That is inverting linearly $(k = 1, 2)$

$$\mu_a'' I_{HN}(\varepsilon_{ag}, \mu_{ag}, d_k, L_k) + \varepsilon_a'' I_{EN}(\varepsilon_{ag}, \mu_{ag}, d_k, L_k) = P_{AN}(\varepsilon_{ag}, \mu_{ag}, d_k, L_k) \tag{37a}$$

and inverting linearly $(k = 1, 2)$

$$\mu_a' I_{HN}(\varepsilon_{ag}, \mu_{ag}, d_k, L_k) - \varepsilon_a' I_{EN}(\varepsilon_{ag}, \mu_{ag}, d_k, L_k) = W_N(\varepsilon_{ag}, \mu_{ag}, d_k, L_k) = W_N^{\text{num}} + W_N^{\text{spar}} \tag{37b}$$

where μ_{ag} and ε_{ag} are approximate guesses of the sample material parameters μ, and ε and μ_g, ε_g are the inverted values. The ε', ε'', μ', and μ'' determination proceeds by (1) placing in the P_{AN} and W_N^{spar} terms the measured S-parameters S_{11}^M and S_{21}^M from the experiment, (2) calculating $I_{HN}(\varepsilon_{ag}, \mu_{ag}, d_k, L_k)$, $I_{EN}(\varepsilon_{ag}, \mu_{ag}, d_k, L_k)$ and $W_N^{\text{num}}(\varepsilon_{ag}, \mu_{ag}, d_k, L_k)$ numerically, and (3) carrying out the 2×2 inversion.

These equations can be useful for helping to determine ε', ε'', μ', and μ'' in several ways: First, if (31) has been minimized and a fairly good approximate value of ε_{ag}', ε_{ag}'', μ_{ag}', and μ_{ag}'' has been found, these equations can be inverted for the parameters ε_a', ε_a'', μ_a', and μ_a'' to check the consistency against the parameter values found from the S-parameter error in minimization. Second, if many 2×2 inversions are made for a wide range of values of L and d, any noise present in the measured data S_{11}^M and S_{21}^M may be averaged out. Third, the equations may be useful to rule out false minimums which may occur when minimizing (31). A negative or ridiculous value of the permittivity or permeability values of the sample would immediately rule out those values from the minimum found. Fourth, (35a and b) are useful, as they could be combined with the search algorithm to predict new values of ε', ε'', μ', and μ'' when minimizing (31).

V. Numerical and Experimental Results

In this section, we present some numerical and experimental results of the theory presented in Sections II, III, and IV.

Fig. 1 shows a plot of the real and imaginary parts of the first three PFW modes normalized propagation coefficients as determined from (4) for values typical of a RAM sample which was tested experimentally (Fig. 4). Fig. 1 inset shows a side and front view of the rectangular waveguide geometry containing the material sample. The PFW modes propagate in Region (b). All coordinates and dimensions in the inset (and in all insets in this paper) are dimensionless and given by (1). The roots γ_{bn} were determined numerically by solving (4) for γ_{bn}^2 using the IMSL package ZANLY and then taking the square root of γ_{bn}^2. In order to insure that all modes were found, the TE_{1n}, γ_{bn} roots of a filled waveguide (FW) were first computed, and for a given mode this root was used as an initialization point to find the PFW mode. In most cases, the TE_{1n}, γ_{bn} initialization root was not close enough to the associated PFW γ_{bn} value in order to find the associated PFW root using the IMSL MATH/LIBRARY package ZANLY. The authors overcame this initialization problem by placing in the PFW values for ε_{b2} and μ_{b2} which were initially close to those of the FW case (that is $\varepsilon_{b2} \cong \varepsilon_{b1}$ and $\mu_{b2} \cong \mu_{b1}$), then calculating the γ_{bn} roots of this case and using these new roots as new initialization points. By repeating this process many times, each time moving ε_{b2} and μ_{b2} closer to that of free space, it was possible to find a smooth root transition to the final PFW root γ_{bn} which was desired. The points marked "+" in Fig. 1 show the TE_{1n}, γ_{bn} FW initialization points, and the points marked with "*" show the final PFW root γ_{bn}. The starred line between the "+" and "*" show many intermediate PFW roots for values of ε_{b2} and μ_{b2} which are intermediate between the FW case $(\varepsilon_{b2} \cong \varepsilon_{b1})$ and $(\mu_{b2} \cong \mu_{b1})$ and the final PFW case when Region (b1) is free space $(\varepsilon_{b2} = 1, \mu_{b2} = 1)$. As can be seen, a smooth transition occurs between the FW and PFW cases, thus guaranteeing that all PFW modes have been found. In the numerical case shown, $\tilde{b} = 3.556$ mm, thus because $\tilde{b} = 2.8$ mm $> \frac{\tilde{b}}{2}$, it was logical to start the overall initialization from an FW initialization point. When $\tilde{d} < \frac{\tilde{b}}{2}$, the same procedure as just described can be used, except that an unfilled waveguide can be used to initialize the root finding procedure. Despite the many PFW roots found (moving from the FW to final PFW modes), the procedure is extremely quick numerically. The procedure also guarantees that all PFW propagating modes are found. For the case shown, 14 modes in all were calculated (Fig. 1 shows only three of these). These modes were found to satisfy the orthogonality criteria (14) to a very high degree.

Fig. 2 shows the real and imaginary parts of the E_z and H_x EM fields that result at the interfaces of the sample at $y = 0$ and $y = -L$ from $0 \leq z \leq b$ at $x = \frac{a}{2}$ when 14 modes are used to solve (9). In Fig. 2(a) and (b), the dotted line refers to fields evaluated at $y = 0^+$ (Region (a) just outside the sample), and the solid line refers to fields evaluated at $y = 0^-$ (Region (b) just inside the sample). In Fig. 2(c) and (d), the dotted line refers to fields evaluated at $y = -L^-$ (just outside the sample), and the solid line refers to fields evaluated at $y = -L^+$. As can be seen from Fig. 2(a)–(d), there is excellent agreement of the E_z and H_x fields at the interface. The discontinuity in the E_z field at $z = d$, $y = 0^-$ and $y = -L^+$ (see Figs. 1 and 2 insets) (inside the sample) occurs because of the material

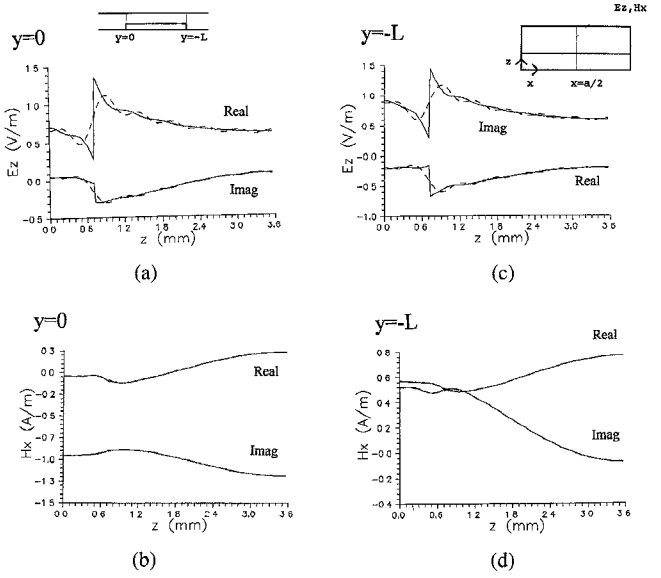

Fig. 2. Plots of the E_z and H_x interface EM fields at $y = 0$ and $y = -L$ is shown as calculated along the line $x = a/2$. In these figures, $\varepsilon = 4.957 - j.277$, $\mu = 1.236$, $\tilde{a} = 7.112$ mm, $\tilde{b} = 3.556$ mm, $\tilde{d} = .722$ mm, and $\tilde{L} = 5$ mm.

discontinuity at $z = d$ and the fact that the E_z field is normal to the discontinuity at this point. The E_z field at $y = 0^+$ and $y = -L^-$ (outside the sample) is continuous as $z = d$ as it should, since there is no material discontinuity at this point. Its interesting how the modal cosine series of the E_z field in Regions (a) and (c) at $z = d$ and $y = 0^+$ and $y = -L^-$ (just outside the sample), respectively, build up to satisfy the discontinuous boundary conditions at $z = d$ and $y = 0^-$ and $y = -L^+$ (just inside the sample region). The H_x field at $y = 0$ and $y = -L$ is continuous at $z = d$ both inside and outside the sample; thus, its boundary condition is met extremely well. The solid and dotted lines can barely be distinguished from one another.

In this paper, experimental S-parameter measurements (34 GHz $\leq f \leq$ 36 GHz) of a RAM sample which partially fills a waveguide have been made using a Hewlett Packhard 8510 VNA with error correction applied. The RAM sample tested was an artificial dielectric which consisted of a rubbery, dark dielectric matrix material. The exact material makeup of the RAM sample were unknown to the authors because of proprietary reasons. The RAM sample was in the form of a large flat sheet. The RAM sample was approximately 2.8 mm thick over most of its area except for one small region which was approximately 1.09 mm. Experimental S-parameter measurements were made of the RAM sheet for the two thicknesses of $\tilde{d} = 1.09$ mm and $\tilde{d} = 2.8$ mm. The measurements were made in a rectangular waveguide (WR28) whose dimensions were $\tilde{a} = 7.112$ mm and $\tilde{b} = 3.556$ mm. S-parameter measurements for the $\tilde{d} = 1.09$ mm thickness were made on 12 strips of the 1.09 mm portion of the RAM sheet (width 7.112 mm, length ranging from 4 mm to 16 mm), and S-parameter measurements for the $\tilde{d} = 2.8$ mm thickness were made on 11 strips of the 2.8 mm portion of the RAM sheet (width 7.112 mm, length ranging from 2–14 mm). All strips were cut from separate parts of the RAM sheet.

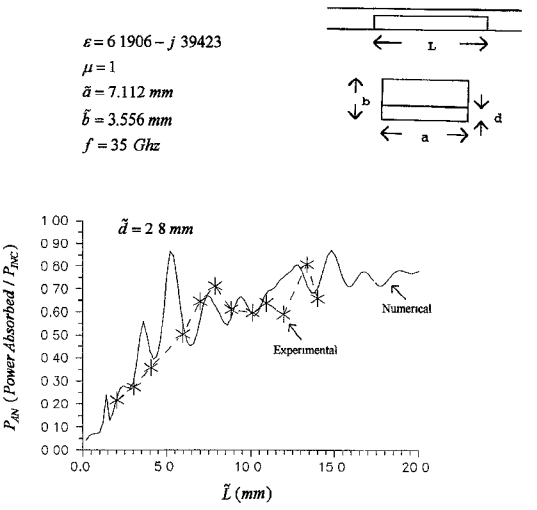

Fig. 3. A comparison of the normalized power absorbed $P_{AN} = Power\ Absorbed/P_{INC}$ is when calculated by the numerical model and when measured when $\tilde{d} = 2.8$ mm.

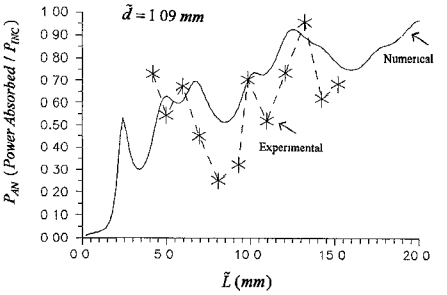

Fig. 4. A comparison of the normalized power absorbed $P_{AN} = Power\ Absorbed/P_{INC}$ is shown when calculated by the numerical model and when measured $\tilde{d} = 1.0922$ mm.

Figs. 3 and 4 show the results of the measurements. Because the sample strips of the same $\tilde{d}$ were all taken from slightly different places in the RAM sheet (with different $\tilde{\varepsilon}$, $\tilde{\mu}$ parameters) and the sample edges may not have been perfectly straight and corners perfectly perpendicular, and because the strip samples may not have had exactly the same height, the S-parameter data collected appeared to be fairly noisy (Figs. 3 and 4). For this reason, (32) ($P_{AN} = P_A/P_{\text{INC}} = 1 - |S_{11}|^2 - |S_{21}|^2$), which gives the normalized power absorbed in terms of the S-parameters, was used to numerically model (that is least squares fit ε', ε'', μ', μ'') the experimental data.

Fig. 3 shows a comparison with the experimental P_{AN} versus the modeled numerical P_{AN} (obtained after minimizing (36) using the numerical IMSL MATH/LIBRARY package BCONF). In Fig. 3, the experimental data appears noisy with perhaps a ± 0.1 derivation from point to point. The numerical model appears to fit the experimental data in a reasonable way. Two local maximums occur at approximately 6 and 12 mm in both the experimental and numerical models, and broad local minimums appear at 8 and 16 mm in both the experimental and numerically modeled data. Both the experimental and numerical curves also show an increase in absorbed power as the sample length increases, which is physically to be expected. Four modes were used to extract the numerical

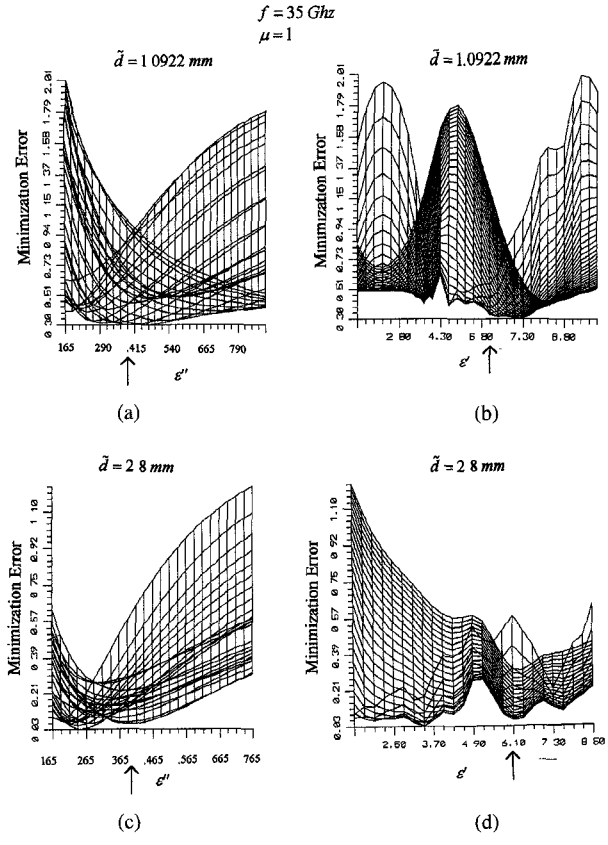

Fig. 5. Plots of the power minimization error are shown as a function of ε' ε''. The arrow shows the point which was taken to be the final minimization point $\varepsilon = 6.1906 - j.39423$.

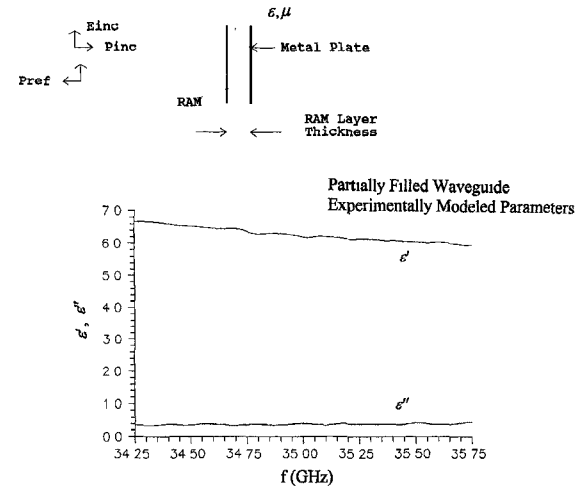

Fig. 6. The experimental modeling parameters ε' and ε'' are shown as a function of frequency.

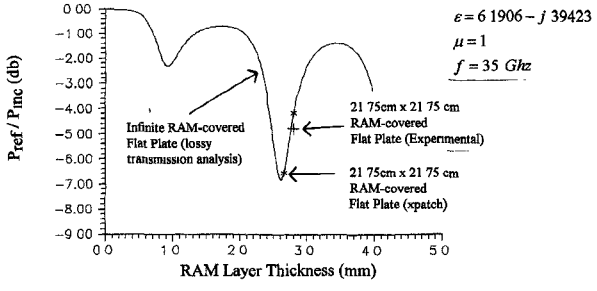

Fig. 7. A plot of normal incidence reflectivity verses RAM layer thickness is shown at $f = 35$. GHz for a RAM layer whose permittivity was modeled from the data in Figs. 3–6.

model shown, and 14 modes were used to plot the curve shown in Fig. 3. Virtually no difference in numerical results occurred using either a 4- or 14-mode analysis. Fig. 4 shows a comparison of the experimental and modeled normalized power absorbed when $\tilde{d} = 2.8$ mm. As can be seen from Fig. 4, a fairly good fit between the numerical model and experimental data resulted for this $\tilde{d}$ case. The higher value of $\tilde{d}$ produced more closely spaced resonances in the numerical data than in Fig. 3. The numerical model used 4 modes to model the experimental data of Fig. 4 and 14 modes to make the plot shown in Fig. 4. Conservation of power according to (19) was observed to a high degree of accuracy ($\sim$.03%) for both Figs. 3 and 4.

Fig. 5 shows plots of the minimization error P_{AN}^{err} (32) for $\tilde{d} = 1.09$ mm and $\tilde{d} = 2.8$ mm when the previously described experimental data were modeled numerically. As can be see from the plots, the $\tilde{d} = 2.8$ mm plots show two minima, whereas the $\tilde{d} = 1.09$ mm data show only a single minima. Only the minima marked by the arrow on the figures coincided for both the $\tilde{d} = 1.09$ mm and $\tilde{d} = 2.8$ mm data. This value ($\varepsilon = 6.1 - j.39$, $\mu = 1.$) for $f = 35$ GHz was taken to be the correct modeled experimental value.

Fig. 6 shows a plot $\varepsilon = \varepsilon' - j\varepsilon''$ versus frequency as obtained from modeling the experimental data previously discussed. The plots show that the lossy dielectric constant ε'' is nearly constant with frequency whereas the real part, ε', drops slowly in value from about 6.7 to 5.9 over the frequency range plotted.

The RAM sheet which was experimentally modeled (Figs. 3–6) was placed in contact with a metal plate (21.75 $\times$ 21.75 cm) and the normal incidence radar reflectivity of the system was measured experimentally [20]. The RAM sheet was approximately 2.8 mm thick over most of its area except for a small 4 $\times$ 4 cm patch located near the edge of the sheet, which was about 1.1 mm thick. The measured experimental reflectivity of the system was about $-$ 4.8 dB. Using the PFW experimentally modeled relative complex permittivity and permeabilty values of $\varepsilon = 6.1906 - j.39423$ and $\mu = 1$ at 35 GHz (Figs. 3–6), the normal incidence radar reflectivity of a RAM-covered infinite flat metal plate (thickness $\tilde{d}$) (Fig. 7 inset) was calculated using a lossy transmission line analysis. The normal incidence radar reflectivity of a RAM-covered finite size plate flat metal plate (same size as the expermental plate) was also calculated ($\varepsilon = 6.1906 - j.39423$ and $\mu = 1$ at 35 GHz) using a recently developed diffraction code x-patch [21]. Fig. 7 shows a comparison of the numerical and experimental results. As can be seen from Fig. 7, the transmission line reflectivity shows a reflectivity minimum of about $-$ 7 dB at a layer thickness of $\tilde{d} = 2.6$ mm. Considering the fact that the experimental RAM sheet was not uniform, the agreement between theory and experiment is quite good. An interesting feature of the plot Fig. 7 is the fact that fairly tight

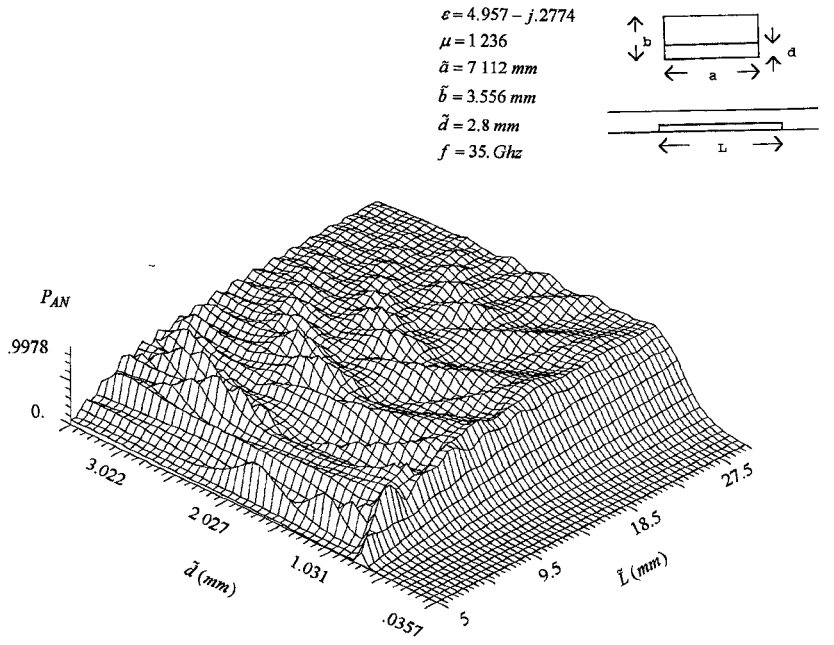

Fig. 8. The normalized power absorbed $P_{AN} = Power\ Absorbed/P_{INC}$ is shown as a function of sample height and sample length.

tolerances on the RAM layer thickness 2.4 mm $\leq \tilde{d} \leq$ 2.8 mm must be maintained in order that the RAM sheet act effectively as radar absorbing sheet at $f = 35$ GHz.

Fig. 8 shows a 3-D plot of the normalized power absorbed versus the layer height $\tilde{d}$ $(0 < \tilde{d} < \tilde{b})$ and $\tilde{L}(0 < 30$ mm) for $f = 35.$ GHz. The values of ε and μ used to model data in Fig. 8 are listed in the Fig. 8 inset. The results of Fig. 8 show that for low values $\tilde{d}$ $(\tilde{d} < 0.75$ mm), that power is absorbed smoothly and slowly into the material with increasing length $\tilde{L}$, where for values of $\tilde{b} \geq \tilde{d} > 0.75$ mm, the power absorbed becomes oscillatory and very dependent on the length, $\tilde{L}$, of the sample. Numerical comparison of the power absorbed when $\tilde{d}$ almost equaled $\tilde{b}$ (Fig. 8), and the case when $\tilde{d} = \tilde{b}$ were made (when $\tilde{d} = \tilde{b}$, this is the filled waveguide case and only a TE_{10} mode propagates in the dielectric sample) and it was found that almost identical power absorbed curves were obtained for the two cases. Overall, Fig. 8 illustrates the type of signature or pattern that can be obtained by varying $\tilde{d}$ and $\tilde{L}$ simultaneously to compare numerical and experimental data.

The dashed curves of Fig. 9(a) show the inversion of (37a) and (37b) when values of $\varepsilon_{ag} = \varepsilon = \varepsilon_a = 5.65 - j.5$ and $\mu_{ag} = \mu = \mu_a = 1.53 - j.5$ (this is considered the exact inversion case since $\varepsilon_{ag} = \varepsilon = \varepsilon_a$) are used to invert (37a) and (37b), and the solid curve shows the result of the inversion when $\varepsilon_{ag} = 5.5 - j.5$, $\varepsilon = 5.65 - j.5$, and $\mu_{ag} = \mu = 1.53 - j.5$ are used to invert (37a) and (37b). (This is considered the approximate inversion case since $\varepsilon \neq \varepsilon_a$.) In the inversion for this case, the terms I_{EN}, I_{HN}, P_{AN}, and W_N^{num} in (37a) and (37b) were evaluated at $\varepsilon_{ag} = 5.5 - j.5$ and $\mu_{ag} = \mu = 1.53 - j.5$, whereas the term W_N^{spar} was evaluated at $\varepsilon_{ag} = \varepsilon = 5.65 - j.5$ and $\mu_{ag} = \mu = 1.53 - j.5$. In the case when the exact values were used to calculate the integrals in (37a) and (37b), an almost exact replication of ε, μ occurred, as can be seen from the flat dashed curves of Fig. 9(a). In the case when only approximate values of ε, μ were used in the integrals in (37a) and (37b), an oscillatory deviation from the true values occurred, as is seen from the solid curves of Fig. 9(a). Despite the approximate integral values used for I_{EN}, I_{HN}, P_{AN}, and W_N, a useful estimate of the $\varepsilon_a \mu_a$ is obtained. Fig. 9(a) and (c) shows plots of the integrals of I_{EN}, I_{HN}, P_{AN}, and W_N, which resulted when exact and approximate values of ε_{ag} and μ_{ag} are used. As can be seen from these figures, the integrals that occur using approximate or exact values are close to each other in value. In Fig. 9(a) $\tilde{d}_1 = \tilde{d}_2 = .13$ mm, and $\tilde{L}_1 = 5.$ mm and 7.5 mm $\leq \tilde{L}_2 \leq$ 17.5 mm. Fourteen modes were used to generate all plots in Fig. 9(b) and (c).

The accuracy of the MOM solution of Section II for the parameter case of Fig. 9 for $\varepsilon = 5.65 - j.5$ and $\mu = 1.53 - j.5$ using 14 modes was checked using the P_{err} formula given by (19) over the sample length range 0.5 mm $\leq \tilde{L} \leq$ 22.5 mm. It was found that when only E_z and H_x field component matching was used $(\rho_{na} = 0,\ \rho_{nc} = 0)$, that the maximum power error that resulted was $P_{\text{err}} = .0355\%$, which occurred at $\tilde{L} = 3$ mm, and the minimum power error that resulted was $P_{\text{err}} = .0154\%$, which occurred at $\tilde{L} = 18.5$ mm. When the E_x, E_z and H_x fields were matched using the Galerkin values of $(\rho_{na} = q_{na},\ \rho_{nc} = q_{nc})$, it was found that the maximum power error that resulted was $P_{\text{err}} = 19.64\%$, which occurred at $\tilde{L} = 2$ mm, and the minimum power error that occurred was $P_{\text{err}} = 2.09\%$, which occurred at $\tilde{L} = 21.5$ mm. At $\tilde{L} = 5$ mm, the Galerkin power error was $P_{\text{err}} = 10.88\%$ and at $\tilde{L} = 10$ mm it was $P_{\text{err}} = 5.53\%$. Because much lower power error matching results were provided by E_z and H_x field matching than by Galerkin matching, only E_z and H_x field matching was used in this paper. The power error results just given were typical of all cases considered by the authors.

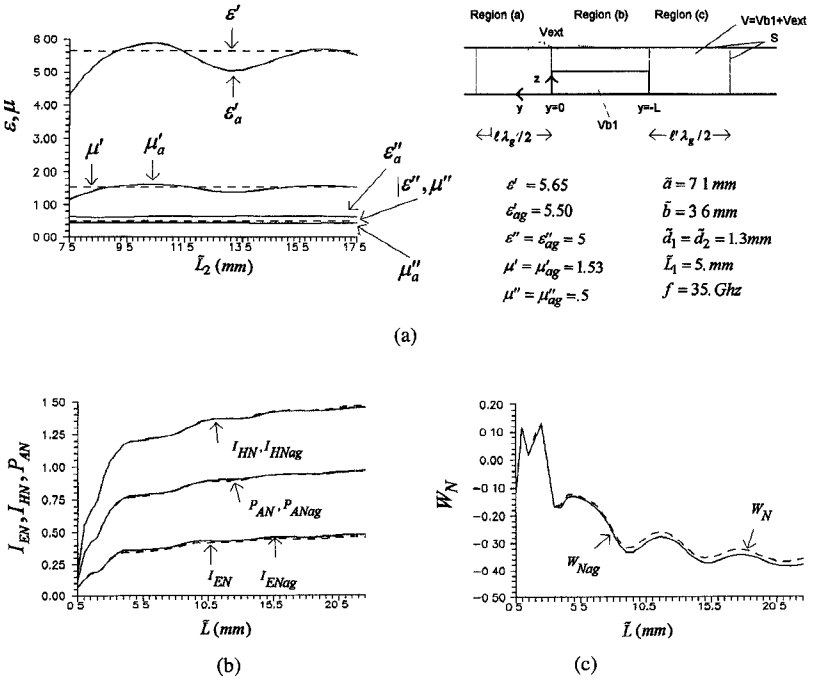

Fig. 9. The parameter inversion, based on (35)–(39), is shown.

The variational solution of Section III was checked numerically for the case when $\varepsilon = 5.65 - .5$, $\mu = 1.53 - j.5$, and $\tilde{L} = 5.$ mm the other parameters were those given in Fig. 9. It was found that the variational solution for this case agreed with the MOM (using E_z and H_x field component matching $(\rho_{na} = 0,\ \rho_{nc} = 0)$) solution to a high degree of accuracy.

The exact inversion case analysis of ε and μ displayed by the dashed curve of Fig. 9(a) serves as an extremely good independent cross-check of the MOM solution and the variational solution presented in Sections II and III, respectively. It is an extremely good cross-check because the MOM solution and variational solutions of Sections II and III depend only on the enforcement of the E_z and H_x elctromagnetic field boundary conditions at $y = 0$ and $y = -L$, whereas a cross-check of the Complex Poynting Theorem requires that all the nonzero EM field compnonents be integrated over the volume $V = V_{b1} + V_{\text{ext}}$ (Fig. 9 inset) as prescribed by the energy and power integrals of (35)–(39). The high degree to which ε and μ are correctly inverted in the exact inversion case of the dashed curved of Fig. 9(a) (ε and μ in the dashed curve of Fig. 9(a) deviates approximately only 1 part in 10^{-4} from the assumed exact values given) demonstrates the high degree of numerical accuracy to which the Complex Poynting Theorem is being obeyed and thus the accuracy to which the EM fields of the overall system are being computed.

VI. Summary and Future Work

In conclusion, a novel method for determining the complex permittivity and permeability of a material at K_a band based on TE_{10} scattering, which occurs from a finite length sample that partially fills a rectangular waveguide, has been presented. The work presented here can also be directly applied to sample analysis at W band. A MOM and a variational solution were developed to determine the EM fields and S-parameters in the waveguide system. The numerical solutions were shown to satisfy to a high degree of accuracy the EM field matching conditions at the sample interfaces, to satisfy the conservation of complex power at the aperture interfaces and satisfy the Complex Poynting Theorem throughout the waveguide system. An experimental analysis of a RAM sample was performed, and its material permittivity and permeability properties were determined by the partially filled waveguide method proposed herein. Normal incidence plane wave experimental reflectivity measurements were made of the RAM material (when it covered a metal plate) and good agreement was found between theoretically predicted reflectivity as calculated using the PFW method proposed in the paper and the experimental results.

The are several ways that the present research work can be extended to analyze more general waveguide cases. First, if the material sample that partially fills the waveguide is longitudinally inhomogeneous ($\varepsilon = \varepsilon(y)$, $\mu = \mu(y)$ in the coordinate system of Fig. 1 inset), a MOM and variational solution for this case may be developed by 1) dividing the inhomogeneous sample into thin longitudinal slabs (each slab is assumed to have uniform ε and μ parameters); 2) matching EM boundary conditions from interface to interface; and 3) solving the resulting matrix equations for the forward and backward propagating modes in each section and for the overall EM fields in the whole system.

A second more general waveguide case that can be analyzed is if the material sample that partially fills the waveguide is vertically inhomogeneous ($\varepsilon = \varepsilon(z)$, $\mu = \mu(z)$ in the coordinate system of Fig. 1 inset). This case may be analyzed by determining the PFW modes of the system by the method proposed by [15] and [16], and then carrying out field matching at the sample interfaces ($y = 0$ and $y = -L$), as has already

been performed in this paper to find a MOM and variational solution to the overall problem. The authors feel that, if the sample had an unknown vertical inhomogeneous profile, the proposed solution would be an ideal one for which an inverse scattering analysis of the unknown profile could be carried out. The magnitude and phase of S_{11} and S_{21} would probably be very sensitive to the vertical inhomogeneous profile, and thus observation of S_{11} and S_{21} would allow determination of the profile. An analysis of the type just mentioned could be important to the design of radar absorbing materials since fabrication process in general may lead to nonuniform RAM sheets.

A third generalization of the research would be to place metal caps (aluminum foil, for example) over the endfaces of the material sample that partially fills the waveguide. This would cause the material sample and endcaps to behave as a partially filled Fabry-Perot resonator. The analysis would be carried out in the same way as already presented in Sections II and III except that the analysis would require that the tangental electric fields at the metal caps be zero. The metal caps placed over the sample endfaces would make the waveguide system much more resonant and possibly increase the sensitivity of the measurement system to the sample material parameters ε and μ.

A fourth generalization of the work would be to analyze the PFW when the material transversely partially fills the waveguide (in the x direction of Fig. 1 inset) rather that the vertical z direction, as has been analyzed here. This case would require a TE_z (Transverse Electric) vector potential analysis [1] using the theory of Sections II and III rather than a TM_z analysis, as has already been presented. Parameter determination based on a TE_z and a TM_z analysis would provide a great deal of data from which to ascertain the ε and μ parameters of the system.

A fifth area of research would be to partially fill the waveguide with chiral material [22]–[24] (these materials are useful as radar absorbers) and from scattering parameters to determine the chiral parameters of the material.

REFERENCES

[1] R. F. Harrington, *Time-Harmonic Electromagnetic Fields*. New York: McGraw-Hill, 1961.

[2] D. Blackham, "Free space characterization of materials," in *Proc. 1993 Antenna Meas. Tech. Assoc. Mtg. & Symp.*, Oct. 1993.

[3] D. K. Ghodgaonkar, V. V. Varadan, and V. K. Varadan, "Free-space measurement of complex permittivity and complex permeability of magnetic materials at microwave frequencies," *IEEE Trans. Instrum. Meas.*, vol. 39, no. 2, pp. 387–394, Apr. 1990.

[4] B. Rama Rao, "Free-space millimeter-wave measurement of the complex dielectric constant of radome materials using nonlinear least-squares analysis," *IEEE Trans. Instrum. Meas.*, vol. 38, pp. 1534–1537, 1989.

[5] E. Knott, J. Shaeffer, and M. Tuley, *Radar Cross Section*, 2nd ed. Norwood, MA: Artech House, 1993.

[6] R. Ro, "Determination of the electromagnetic properties of Chiral composites using normal incidence measurements," Ph.D. dissertation, Pennsylvania State Univ., University Park, Aug. 1991.

[7] V. V. Varadan, R. D. Hollinger, D. K. Ghodgaonkar, and V. K. Varadan, "Free-space, broadband measurements of high-temperature, complex dielectric properties at microwave frequencies," *IEEE Trans. Instrum. Meas.*, vol. 40, no. 5, pp. 842–846, Oct. 1991.

[8] D. K. Ghodgaonkar, V. V. Varadan, and V. K. Varadan, "A free-space method for measurement of dielectric constants and loss tangents at microwave frequencies," *IEEE Trans. Instrum. Meas.*, vol. 37, no. 3, pp. 789–793, June 1989.

[9] M. C. Steel, R. J. Sheppard, and R. Collins, "Precision waveguide cells for the measurement of complex permittivity of lossy liquids and biological tissue at 35 GHz," *J. Phys. E: Sci. Instrum.*, vol. 20, pp. 872–877, 1987.

[10] J. M. Alison and R. J. Sheppard, "A precision wave-guide system for the measurement of complex permittivity of lossy liquids and solid tissues in the frequency-range 29-GHz to 90-GHz–III. The liquid-system for 57 to 82-GHz: An investigation into water and formamide," *Meas. Sci. & Technol.*, vol. 2, no. 10, pp. 975–979, 1991.

[11] M. G. M. Richards and R. J. Sheppard, "A precision wave-guide system for the measurement of complex permittivity of lossy liquids and solid tissues in the frequency-range 29-GHz to 90-GHz–II. The liquid-system for 90-GHz, high-frequency cell design," *Meas. Sci. & Technol.*, vol. 2, no. 7, pp. 663–667, 1991.

[12] Hewlett-Packard, "Measuring dielectric constant with the HP 8510 network analyzer—The measurement of both permittivity and permeability of solid materials," *Product Note*, no. 8510-3.

[13] W. Wu and C. E. Smith, "Dielectric measurements using the HP 85070A probe," in *Proc. IEEE Reg. III Southeast Conf. '92*, Apr. 12–15, 1992, pp. 83–86.

[14] J. R. Birch, G. J. Simonis, M. N. Afsar, R. N. Clarke, J. M. Dutta, H. M. Frost, X. Gerbaux, A. Hadni, W. Hall, R. Heidinger, W. W. Ho, C. R. Jones, F. Koniger, R. L. Moore, H. Matsuo, T. Nakano, W. Richter, K. Sakai, M. R. Snead, U. Stumper, R. S. Vigil, and T. B. Wells, "An intercomparison of measurement techniques for the determination of the dielectric properties of solids at near millimeter wavelengths," *IEEE Trans. Microwave Theory Tech.*, vol. 42, no. 6, pp. 956–965, June 1994.

[15] F. E. Gardiol, "Higher-order modes in dielectrically loaded rectangular waveguides," *IEEE Trans. Microwave Theory Tech.*, vol. MTT-16, no. 11, pp. 919–924, Nov. 1968.

[16] R. E. McIntosh and L. J. Turgeon, "Analysis of lossy inhomogeneous waveguide using shooting methods," *IEEE Trans. Microwave Theory Tech.*, pp. 952–954, Nov. 1974.

[17] J. Strube and F. Arndt, "Rigorous hybrid-mode analysis of the transition from rectangular waveguide to shielded dielectric image guide," *IEEE Trans. Microwave Theory Tech.*, vol. MTT-33, no. 5, pp. 391–401, May 1985.

[18] R. E. Collin, *Field Theory of Guided Waves*, sec. 6.1. New York: McGraw-Hill, 1960.

[19] J. Galejs, *Antennas in Inhomogeneous Media*. London: Pergamon, 1969.

[20] J. B. Johnson, Jr., W. S. Albritton, and J. M. Jarem, "Radar cross section prediction of bare and RAM covered objects," in *5th Ann. Ground Target Modeling & Validation Conf.*, Michigan Tech. Univ., Houghton, MI, Aug. 23–25, 1994.

[21] *User Manual for xpatch*, Demaco, Inc., Sept. 15, 1993.

[22] D. L. Jaggard and N. Engheta, "Chirosorb™ as an invisible medium," *Electron. Lett.*, vol. 25, no. 3, pp. 173–174, Feb. 1989.

[23] C. F. Bohren, R. Luebbers, H. S. Langdon, and F. Hunsberger, "Microwave-absorbing chiral composites: Is chirality essential or accidental?" *Appl. Opt.*, vol. 31, no. 30, pp. 6403–6407, Oct. 1992.

[24] V. K. Varadan, V. V. Varadan, and A. Lakhtakia, "On the possibility of designing anti-reflection coatings using chiral composites," *J. Wave-Material Interact.*, vol. 2, no. 1, pp. 71–81, Jan. 1987.

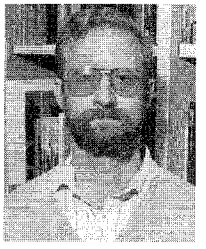

John M. Jarem (M'82–SM'95) received the B.S.E.E., M.S.E.E., and Ph.D. degrees from Drexel University, Philadelphia, PA, in 1971, 1972, and 1975, respectively.

He was Assistant Professor and Associate Professor at the University of Petroleum and Minerals, Dhahran, Saudia Arabia, from 1975 to 1981. From 1981 to 1987, he was Professor of Electrical Engineering at the University of Texas at El Paso. Currently, he is Professor of Electrical and Computer Engineering at the University of Alabama in Huntsville. His research interests are electromagnetics and antenna theory.

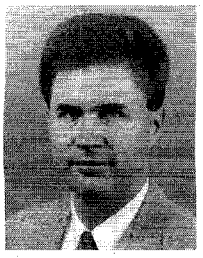

James B. Johnson, Jr. (M'91) was born in Athens, AL, in 1965. He received the B.S.E. and M.S.E. degrees from the University of Alabama in Huntsville in 1987 and 1992, respectively.

Since 1987 he has served as an Electronics Engineer for the U.S. Army Redstone Technical Test Center (RTTC). His early work consisted of microcircuit and microwave component testing. Since 1993 he has been Team Leader of RTTC's Radar Systems Group where he is responsible for a variety of U.S. Army radar system test programs. His current research interests are in the areas of millimeter wave (MMW) antenna and radome metrology, MMW virtual test environments, and distributed interactive simulation.

Mr. Johnson received the Department of the Army Achievement Medal for Civilian Service in 1993 and the U.S. Army Test and Evaluation Command Gamble Award for best technical paper in 1994.

W. Scott Albritton (S'91–M'92) was born in Knoxville, TN, Sept. 22, 1969. He received the B.E.E. degree from Auburn University, Alabama, in 1992.

Since joining Amtec Corp. as an Engineer in 1992, he has been involved in microwave/millimeter wave component measurements, antenna measurements, radar cross section measurements and simulations, and system level tests of various U.S. Army systems.